

Landsliding and the evolution of normal-fault-bounded mountains

Alexander L. Densmore

Department of Geology, Trinity College, Dublin, Ireland

Michael A. Ellis

Center for Earthquake Research and Information, University of Memphis, Memphis, Tennessee

Robert S. Anderson

Institute of Tectonics and Department of Earth Sciences, University of California, Santa Cruz

Abstract. Much of the tectonic and climatic history in high-relief regions, such as the mountains of the western U.S. Basin and Range province, is contained in the morphology of hillslopes, drainage networks, and other landforms that range in scale from 10^{-1} to 10^1 km. To understand how these landforms evolve, we have developed a numerical landscape evolution model that combines a detailed tectonic displacement field with a set of physically based geomorphic rules. Bedrock landsliding, long recognized as a significant geomorphic process in mountainous topography, is for the first time explicitly included in the rule set. In a series of numerical experiments, we generate synthetic landscapes that closely resemble mountainous topography observed in the Basin and Range. The production of realistic landscapes depends critically on the presence of bedrock landslides, and landsliding yields rates of long-term erosion that are comparable in magnitude to those of fluvial erosion. The erosive efficiency of bedrock landsliding implies that hillslopes may respond very quickly to changes in local base level and that fluvial erosion is the rate-limiting process in steady state experimental landscapes. Our experiments generate power law distributions of landslide sizes, somewhat similar to both field and laboratory observations. Thus even a simple model of bedrock landsliding is capable of quantitatively reproducing mountainous topography and landslide distributions and represents a significant step forward in our understanding of the evolution of normal-fault-bounded ranges.

1. Introduction

Despite recent interest in the interplay between tectonics and topography [Merritts and Ellis, 1994, and references therein], the evolution of mountainous topography at the landform scale remains poorly understood. While the gross morphology of a particular mountain range or orogen may reflect the large-scale forces that have shaped it [Elliott, 1976; Suppe, 1981; Koons, 1989; Beaumont *et al.*, 1998], additional information on the tectonic and climatic history of the range is contained in landforms that are one to several kilometers in extent, including individual hillslopes and catchments, faceted spurs, and depositional fans.

A numerical model of landscape evolution provides one way to explore the sensitivity of different landforms to tectonic and climatic processes and may be used to compare the relative roles of various processes in shaping the landscape. Most landscape evolution models (LEMs) have focused on orogenic-scale landscapes and have reasonably ignored the finer details of the topography [Koons, 1989; Anderson, 1994; Gilchrist *et al.*, 1994; Kooi and Beaumont, 1994; Tucker and Slingerland, 1994, 1996]. A disadvantage of these orogen-scale LEMs is that they require coarse spatial resolutions and lumped parameter rule sets, which limit the extraction of tangible or measurable in-

formation from the model results. In a high-resolution model like the one we develop here, geomorphic rule sets may be grounded in the physics of specific processes. Landform evolution may then be linked to measurable relative process rates. Recent LEMs have proposed physically based algorithms for the processes of hillslope sediment transport [Anderson, 1994; Rosenbloom and Anderson, 1994], fluvial sediment transport [Howard, 1994], and bedrock channel incision [Howard *et al.*, 1994]. As yet, however, no LEM has incorporated realistic algorithms for tectonic displacements or bedrock landsliding. We discuss below why such algorithms are important in generate and interpreting mountainous landforms, and our reasons for applying the completed LEM to mountainous topography in the Basin and Range province of the western United States.

1.1. Models of Tectonic Displacements

Coseismic and aseismic tectonic displacements generate structural relief and create the template on which geomorphic processes act. The degree of realism required in the tectonic displacement field used by an LEM depends on the desired realism and spatial resolution of the model. Simple wedge-shaped [Kooi and Beaumont, 1996], sinusoidal [Tucker and Slingerland, 1996], or Gaussian [Anderson, 1994] uplift patterns may be sufficient to simulate orogenic-scale tectonic displacements. At higher resolutions, permanent tectonic displacement fields generally display significant structure at length scales of a few kilometers [e.g., King *et al.*, 1988; Stein *et al.*, 1988]. If

Copyright 1998 by the American Geophysical Union.

Paper number 98JB00510.
0148-0227/98/98JB-00510\$09.00

topography is generated by repeated applications of that displacement field, simulating the effects of multiple earthquakes on a particular set of faults, then a high-resolution LEM must include a tectonic function that accurately reproduces structure in the displacement field at those length scales.

1.2. Models of Bedrock Landsliding

Bedrock landsliding has been shown to be a significant geomorphic process in a variety of landscapes [Kelsey, 1980, 1988; Pearce and Watson, 1986; Schmidt and Montgomery, 1995; Blodgett et al., 1996; Burbank et al., 1996; Densmore et al., 1997; Hovius et al., 1997]. Blodgett et al. [1996] calculated short-term erosion rates due to landsliding of 10–14 mm yr⁻¹ in the Bolivian Andes, while Hovius et al. [1997] derived erosion rates of 5–12 mm yr⁻¹ in the Southern Alps of New Zealand. Despite these observations the long-term role of bedrock landslides in landscape evolution is poorly understood, and no LEM has yet incorporated a realistic bedrock landsliding mechanism. Existing LEMs treat hillslope processes either as diffusive [e.g., Kooi and Beaumont, 1994, 1996], or as a “buzz saw” that instantaneously lowers unstable slopes [Howard, 1994; Tucker and Slingerland, 1994]. Anderson [1994] argued that bedrock landslides are necessary to produce the linear hillslopes often observed in real landscapes, and simulated the landslide process with a hillslope sediment flux that increased sharply as a critical slope angle was approached. These approaches have been shown to produce realistic-looking landscapes and may be sufficient if the modeling goal is simply to reproduce the gross shape of the topography. However, they are ultimately limited by their reliance on parameters that have no physical meaning: a “landscape-scale” diffusivity in the case of the diffusion model, and a critical slope threshold in the case of the buzz saw model. In addition, such deterministic models ignore the potentially important and time-dependent role played by large bedrock landslides in landscape evolution. For example, large landslides may form natural dams whose creation and eventual failure have drastic impacts on the downstream geomorphology of the river system [Costa and Schuster, 1988]. The size of the landslide dam determines both how long it persists and how large the eventual outburst flood is, which in turn determine the amount of geomorphic change effected by the presence of the dam [Costa and O'Connor, 1995]. Finally, such deterministic models cannot be used in testing frequency-magnitude distributions of landslides, despite the fact that these distributions provide a distinctive fingerprint of mountainous regions and are increasingly easy to acquire through remote sensing [e.g., Hovius et al., 1997].

A variety of studies have addressed either the short-term behavior of bedrock landslides or their spatial and temporal distribution. Selby [1980] recognized the importance of discontinuities in controlling and material properties of bedrock and devised a landscape-scale bedrock strength index. Kirkby [1987] produced one-dimensional numerical models of hillslope evolution by landsliding using a steady state reaction model. Schmidt and Montgomery [1995] used the observed relief in landslide-dominated regions to infer landscape-scale bedrock strength, and Miller and Dunne [1996] predicted the two-dimensional density of fracturing within bedrock hillslopes. Compilations of spatial landslide distributions have generally been limited to small spatial and temporal scales [e.g., Megahan et al., 1978; Noever, 1993], although a number of recent studies have used remote-sensing techniques to determine landscape-scale landslide scaling laws and erosion rates

[Pearce and Watson, 1986; Blodgett et al., 1996; Hovius et al., 1997].

1.3. Application to the Basin and Range Province

The primary motivation behind the development of our LEM is to explore the evolution of mountainous topography in the Basin and Range province as a function of both surface and tectonic processes. The dramatic ranges of the Basin and Range are consequences of late Cenozoic extension and have inspired eloquent explanations for the origin of mountains in general. The structure of these ranges is due to time-integrated tectonic displacements, and consequently, their structural geology has received the most attention in resolving issues about their origin. In contrast, their topography has received little attention since the turn of the century [Gilbert, 1928] (see Sharp [1939, 1940] and Wallace [1978] for notable exceptions). This is partly because mountainous topography is often considered the remnant of the more active process of geological mountain building, the insignificant remains of the day. Even when topography is acknowledged to contain valuable tectonic information, it is recognized that this information is convolved with the effects of surface processes. We show that despite this, the topography of actively forming mountains may yield quantitative insights into both sets of processes.

In this paper, we describe a numeric landscape evolution model and demonstrate the role of bedrock landsliding in the evolution of synthetic landscapes at length scales of 10²–10⁴ m. Since this is, to our knowledge, the first LEM to incorporate a bedrock landsliding rule, we compare our model predictions of topography, landslide erosion rates, and landslide distribution with existing field data from active-fault-bounded mountains in the Basin and Range.

2. The Landscape Evolution Model: ZSCAPE

ZSCAPE is a three-dimensional numerical model that acts on a finite-difference grid [Ellis et al., 1995]. We use a 100-m spacing between grid points as a compromise between spatial resolution and computation time. This is comparable to the resolution of the U.S. Geological Survey (USGS) 3-arcsec digital elevation models (DEMs), and we test our numerical landscapes against those digital data. The model processes can be divided into two distinct groups: a tectonic rule set, which generates a bedrock displacement field, and a geomorphic rule set, which attacks the resulting bedrock topography and rearranges mass at the surface.

3. Tectonic Rule Set

Current LEMs use a kinematic tectonic forcing function that prescribes a relatively simple pattern of uplift assumed to be appropriate at the temporal and length scale of interest. In most cases, these LEMs have been aimed at very long-term ($\geq 10^6$ years) and long length scale ($\geq 10^5$ m) orogens in which the details of tectonic displacements due to upper crustal faulting are likely to be irrelevant. Our level of interest, however, is at the mountain range scale and below, which requires a more realistic tectonic displacement function.

We assume that patterns of deformation are derived primarily from the sum of repeated earthquakes across faults within the upper crust [Stein et al., 1988; King et al., 1988], and we assume that such displacement fields may be derived from planar dislocations within an isotropic elastic half-space. A

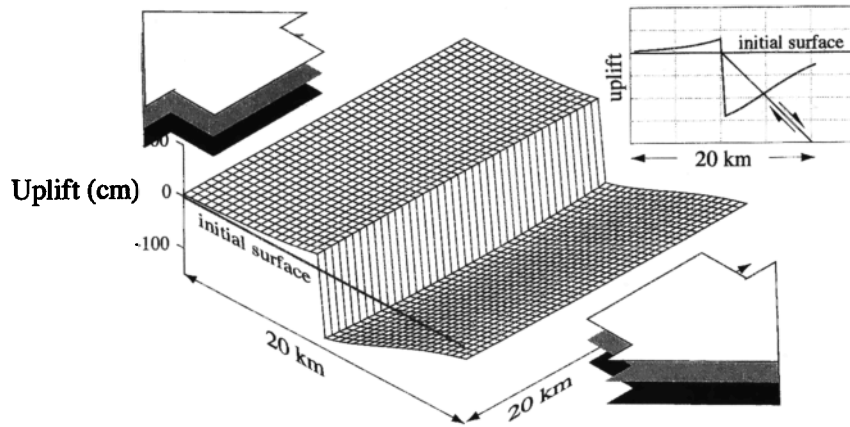


Figure 1. Tectonic displacement field used in the model experiments, corresponding to a single earthquake ($M_w \sim 7.0$). The fault is driven by a pure shear, extensional displacement gradient tensor (shown schematically by the large arrows) at a strain rate of $\sim 10^{-7} \text{ yr}^{-1}$. Note that the fault extends along strike beyond the edges of the 20 by 20 km displacement field. The ZSCAPE experiments use only the central 10 by 10 km region of the displacement field shown here. The inset shows a cross section through the center of the displacement field, as well as the 45°-dipping fault plane.

number of studies have demonstrated that simple elastic dislocation models reproduce at least the first-order features of real tectonic displacement fields from a variety of geologic settings [e.g., Stein *et al.*, 1988; Massonnet *et al.*, 1993; Gomberg and Ellis, 1994; Anderson and Menking, 1994].

We calculate displacements using the three-dimensional boundary-element algorithm of Gomberg and Ellis [1993, 1994], based on the three-dimensional Green's function of Okada [1992]. The boundary element method [Crouch and Starfield, 1983] provides analytical solutions for displacements within a material that is subject to internal displacements across one or more planar dislocation elements. Solutions are obtained by minimizing strain energy within the material while satisfying stress, strain, or displacement boundary conditions. The Gomberg-Ellis algorithm allows in addition the specification of a remote or far-field boundary condition that provides the driving force for displacements across model faults that are constrained by stress conditions.

In the present experiments, we drive displacements across normal faults by specifying a regional pure shear in which crust is horizontally extended at twice the magnitude that it is thinned vertically and shortened horizontally. For a 45°-dipping fault of 40-km length and 15-km width (down-dip), this increment of pure shear yields displacements that correspond to an earthquake of moment magnitude 7.0 (Figure 1). We repeat these earthquakes at 500 year intervals, which corresponds to a strain-rate of 10^{-7} yr^{-1} over a length of 100 km. These figures are within an order of magnitude of current estimates of strain across the Basin and Range province [Savage *et al.*, 1995; Dixon *et al.*, 1995].

Surface displacements due to the model earthquake range from 140 cm of subsidence to 30 cm of uplift. We neglect second-order displacements due to postseismic processes that result from the viscous relaxation of stresses in lower crustal material. At present, the model does not allow for flexural isostatic elevation changes that result from differential loading and unloading. These changes have been shown to be significant in extensional settings [e.g., Weissel and Karner, 1989; King and Ellis, 1990; Small and Anderson, 1995]. We demonstrate below, however, that the differential flexural change in eleva-

tion across our 10 by 10 km model space is small for geologically reasonable values of crustal elastic thickness. Flexurally derived tilting, which could potentially influence the geomorphic evolution of the model space, is thus relatively unimportant.

The accumulation of tectonic deformation importantly involves both horizontal and vertical displacements. Many three-dimensional LEMs incorporate only vertical displacements, but we employ the full three-dimensional field. We use an Eulerian description of the deformation that amounts to watching material move through the fixed finite-difference grid.

4. Geomorphic Rule Set

Erosion and deposition within the model are dictated by conservation of mass, which relates the rate of change of the surface elevation to spatial gradients in sediment flux:

$$\partial z / \partial t = (1/\rho) \nabla \cdot q_s \quad (1)$$

Here $\partial z / \partial t$ is the rate of elevation change with time, ρ is the bulk density of the material in question, and q_s is the mass sediment transport rate per unit width. (These and other symbols are depicted in the notation section.) In determining numerical expressions for q_s , most surface processes models have distinguished between hillslope and fluvial sediment transport processes [Anderson, 1994; Howard, 1994; Tucker and Slingerland, 1994; Kooi and Beaumont, 1996]. We take a similar approach, identifying four key geomorphic processes active in the Basin and Range: regolith production, regolith transport, bedrock landsliding, and fluvial sediment transport. The first three processes occur on hillslopes, while the last is confined to the fluvial channel system. To accommodate this basic dichotomy, we divide the landscape into hillslope and channel nodes and apply the appropriate algorithms to each set of nodes. While we recognize that valley glaciers have been important geomorphic agents in parts of the highest ranges of the Basin and Range [e.g., Stewart, 1980], we ignore their effects in our current experiments.

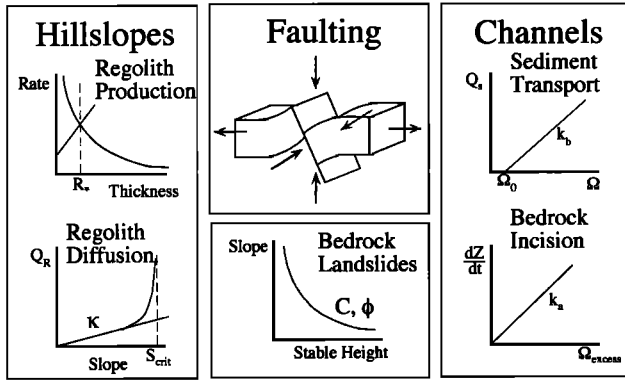


Figure 2. Schematic diagram of the tectonic and geomorphic components of the ZSCAPE rule set. Topography is produced by faulting in response to an applied displacement gradient tensor. Regolith is produced at all nodes in the model space and is transported via a linear diffusion law that accounts for shallow mass movements. Bedrock landsliding is controlled by a stochastic law that depends upon the maximum stable hill-slope height, which in turn is determined by the rock cohesion and friction angle. Channel nodes are defined on the basis of excess stream power, which also dictates the rate of alluvial sediment transport and the rate of bedrock incision.

Because of constraints on computation time, LEMs in general are incapable of resolving the effects of geomorphic processes below some cutoff length scale. The magnitude of this length scale depends on the particular numerical algorithm used to represent the process in question. ZSCAPE is not immune to this cutoff, but we have tried to represent the key geomorphic processes with algorithms that allow us to extend the cutoff down to length scales of the order of 100 m. In this way we are able to examine the landscape at the scale of individual landforms. Our experiments are not intended to reproduce the fine-scale details of the topography, such as the detailed morphology of a stream bed or the effect of jointing on an individual bedrock landslide [Weissel and Seidl, 1997]. Rather, they are designed to bridge the gap between orogenic-scale simulations, in which geomorphic processes are only crudely represented, and landform-scale analyses, which ignore the larger spatial and temporal framework.

4.1. Regolith Production

Sediment transport requires the presence of a mobile layer of regolith, distinct from the bedrock. The regolith thickness is defined as the difference between the surface and bedrock elevations. Regolith is produced by in situ weathering of bedrock, which lowers the bedrock surface elevation and increases the regolith thickness. Since weathering processes are partly dependent on the presence of water at the bedrock surface for significant periods of time, peak regolith production rates have been hypothesized to occur beneath some finite thickness of regolith, rather than on bare bedrock [Ahnert, 1970]. Recent studies using cosmogenic radionuclide concentrations have confirmed that weathering is faster beneath regolith than on bare bedrock [Small and Anderson, 1996] and that regolith production rates decline rapidly beneath thicker regolith [Hemmsath et al., 1996]. The exact dependence of the production rate curve on regolith thickness is poorly known.

We adopt a linear increase in regolith production rate, $\partial R/$

∂t , up to a regolith thickness R_* , beyond which the rate declines exponentially (Figure 2):

$$\frac{\partial R}{\partial t} = \left(\frac{\partial R}{\partial t} \right)_0 + \left[\frac{(\partial R/\partial t)_* - (\partial R/\partial t)_0}{(\partial R/\partial t)_*} \right] R \quad (2)$$

$$0 \leq R \leq R_*$$

$$\frac{\partial R}{\partial t} = \left(\frac{\partial R}{\partial t} \right)_* \exp \left[\frac{R_* - R}{R_{\text{scale}}} \right] \quad R > R_* \quad (3)$$

Here R is the regolith thickness, $(\partial R/\partial t)_0$ is the bare bedrock regolith production rate, $(\partial R/\partial t)_*$ is the maximum production rate at thickness R_* , and R_{scale} is the exponential decay length scale (Table 1). Regolith production rates on bare bedrock in the western United States, determined by cosmogenic radionuclide concentrations, are typically $10\text{--}50 \times 10^{-6} \text{ m yr}^{-1}$ [e.g., Bierman, 1994; Small and Anderson, 1996].

4.2. Regolith Transport

Hillslope transport of regolith typically occurs by processes such as creep, slope wash, rain splash, and downslope motion due to animal activity [Selby, 1993]. Since the transport rates produced by these processes are slope-dependent, we model regolith transport as a linear diffusive process (Figure 2):

$$q_s = -k \nabla \cdot z \quad (4)$$

where k is a diffusion coefficient. Combining equations (1) and (2) yields a diffusion equation for topography:

$$\partial z/\partial t = \kappa \nabla^2 z \quad (5)$$

Here $\partial z/\partial t$ is the rate of change of the surface elevation and κ is the topographic diffusivity (equivalent to k/ρ). Typical landform-scale diffusivities calculated for semiarid to arid landscapes in the western United States are $0.01 \text{ m}^2 \text{ yr}^{-1}$ [Hanks et al., 1984; Rosenbloom and Anderson, 1994]. While some LEMs have used diffusional algorithms, with dramatically greater diffusivities, to produce realistic-looking topography [Koons, 1989; Kooi and Beaumont, 1994], we note again that diffusion is properly applied only to transport-limited processes [Ander-

Table 1. Model Parameters

Parameter	Value	Reference
β_{crit}	34°	...
C	$6 \times 10^4 \text{ kg m}^{-1} \text{ s}^{-2}$ (2×10^7 in experiment 5)	1
Δt	10 years	...
Δx	100 m	...
γ	$2.7 \times 10^4 \text{ kg m}^{-2} \text{ s}^{-2}$...
κ	$0.01 \text{ m}^2 \text{ yr}^{-1}$	2,3
k_a	$1.6 \times 10^{-4} \text{ m}^2 \text{ s}^2 \text{ kg}^{-1}$	visual inspection
k_b	$1.2 \times 10^{-7} \text{ m s}^2 \text{ kg}^{-1}$	4; visual inspection
k_w	8.0×10^{-4}	visual inspection
Ω_0	$4 \times 10^5 \text{ kg s}^{-3}$	visual inspection
P	1 m yr^{-1}	...
ϕ	17° (40° in experiment 5)	1
$(\partial R/\partial t)_0$	$1 \times 10^{-5} \text{ m yr}^{-1}$	5
$(\partial R/\partial t)_*$	$5 \times 10^{-5} \text{ m yr}^{-1}$	6
τ_r	500 years	...

References are as follows: 1, Schmidt and Montgomery [1995]; 2, Hanks et al. [1984]; 3, Rosenbloom and Anderson [1994]; 4, Stock and Montgomery [1995]; 5, Small and Anderson [1996]; and 6, E. E. Small (unpublished data, 1996).

son and Humphrey, 1989] and that its efficacy in shaping the landscape is contingent upon the availability of regolith.

The diffusion equation ignores any potential for advective transport of regolith, for example by shallow landsliding. To address this, we follow Anderson [1994] in simulating regolith mass movement by allowing the sediment transport rate q_s to increase exponentially as a critical topographic slope β_{crit} is approached (Figure 2; Table 1). While this is an approximate solution, we show below that rates of weathering-limited processes such as diffusion are dwarfed by rates of fluvial and landsliding processes in the arid landscapes in which we are interested.

4.3. Fluvial Sediment Transport

We distinguish between alluvial and bedrock channel behavior depending on the availability of mobile material within the channel. Potential fluvial sediment transport flux is assumed to be proportional to the available stream power per unit bed area, Ω [Bagnold, 1977], approximated here as

$$\Omega = \frac{\gamma APC_r S}{w} \quad (6)$$

where γ is the flow unit weight, A is the contributing drainage area, P is the precipitation rate, C_r is the runoff coefficient, S is the channel bed slope, and w is the flow width (Table 1). The precipitation rate is set to 1 m yr^{-1} and is both spatially and temporally constant in these experiments (Table 1). Since our grid spacing (100 m) is much greater than typical flow widths, we use an empirical relation between flow width and contributing drainage area,

$$w = k_w \cdot \sqrt{A} \quad (7)$$

where k_w is the empirically determined constant (Table 1).

The channel network is defined as the set of nodes for which $\Omega \geq \Omega_0$, where Ω_0 is the threshold stream power necessary for channel initiation [Bagnold, 1977]. We follow Bagnold [1977] in relating alluvial sediment transport flux to excess stream power:

$$Q_s = k_a \cdot (\Omega - \Omega_0) \quad (8)$$

where Q_s is the potential volumetric sediment transport rate per unit bed width and k_a is an empirical proportionality constant (Figure 2; Table 1). Spatial gradients in sediment transport dictate the rate of change of the bed elevation, as given by equation (1). Any excess stream power, defined as the available power beyond that required to transport all sediment in a particular node, erodes the bedrock channel bed [e.g., Seidl and Dietrich, 1992] at a rate given by

$$\frac{\partial z_b}{\partial t} = k_b \cdot \Omega_{\text{excess}} \quad (9)$$

where k_b is an empirical proportionality constant and Ω_{excess} is the excess stream power (Figure 2; Table 1).

The behavior of alluvial and bedrock channels in our model is thus prescribed primarily by the empirical parameters k_a , k_b , and Ω_0 . While some effort has gone toward general characterizations of these parameters [e.g., Bagnold, 1977; Rosenbloom and Anderson, 1994; Stock and Montgomery, 1995], differences in the algorithms used by different workers make such generalization difficult. We have chosen parameter values by letting ZSCAPE operate on DEM representations of real to-

pography from several mountain ranges in the Basin and Range. We thus generate synthetic channel networks whose spatial extent depends on Ω_0 and whose rates of sediment transport and bed incision depend upon k_a and k_b . By comparing these results with observed channel networks and typical transport and incision rates, we can determine reasonable values of these parameters. Sensitivity tests demonstrate that our experimental results cannot discriminate between values that differ by less than an order of magnitude.

Finally, we note that our chosen precipitation rate (1.0 m yr^{-1}) is considerably higher than measured historical rates from the Basin and Range (typically $<0.5 \text{ m yr}^{-1}$). Precipitation rates during the last glacial maximum are estimated to be 30–100% higher than present, although there is considerable disagreement over the magnitude of the change [Spaulding, 1985]. We stress that our chosen value is somewhat arbitrary, since precipitation is linearly related to sediment transport and bed incision through the empirical parameters k_a and k_b , which are chosen on the basis of landscape form. While absolute values of precipitation are relatively unimportant from this perspective, relative temporal changes in precipitation may play an important role in landscape evolution; we do not explore this issue here.

4.4. Bedrock Landsliding

The final geomorphic component of the model is a bedrock landsliding algorithm, which determines the distribution of landslides in both space and time. In natural settings, landslide occurrence is strongly stochastic, and we argue that a realistic algorithm must reflect this stochastic character. Discrete bedrock landslides deliver large and highly spatially variable amounts of sediment to the channel network, affecting the pattern of erosion and deposition within the channel and thus its geomorphic evolution. The frequency and magnitude of the landslide events control this evolution [Wolman and Miller, 1960], as does the sequence in which the events occur [Densmore et al., 1997]. Accurate simulation of the landscape requires a representation of the landslide process that captures the essence of the observed long-term behavior.

A bedrock landsliding algorithm must address four central issues: where landslides begin, when they occur, how large they are, and where the landslide material ends up after failure. We use the terms bedrock landslide and landslide interchangeably to denote a mass movement that involves intact or unweathered bedrock rather than being confined to a mobile regolith layer.

In the absence of strong tectonic and climatic variations, landslides in natural settings are concentrated on hillslopes that experience a fall in local base level. This base level drop may be due to vertical motion across a fault, to the occurrence of a separate landslide lower on the hillslope [Densmore et al., 1997], or to incision by a glacier [Harbor, 1992] or stream [Megahan et al., 1978; Kelsey, 1980, 1988; Seidl et al., 1996; Densmore et al., 1997]. Landslides are often observed to cluster near the toes of hillslopes [Megahan et al., 1978; Kelsey, 1988; Densmore et al., 1997]. Megahan et al. [1978] found that most landslides in the Northern Rocky Mountain physiographic province occurred on the lower one third of the hillslope. Kelsey [1988] found that most landslides along Redwood Creek, California, initiated at the base of the slope, leading to the formation of a steep toe or inner gorge along the channel. Densmore et al. [1997] observed that all slides on a granular model hillslope initiated at the toe and that 90% involved only

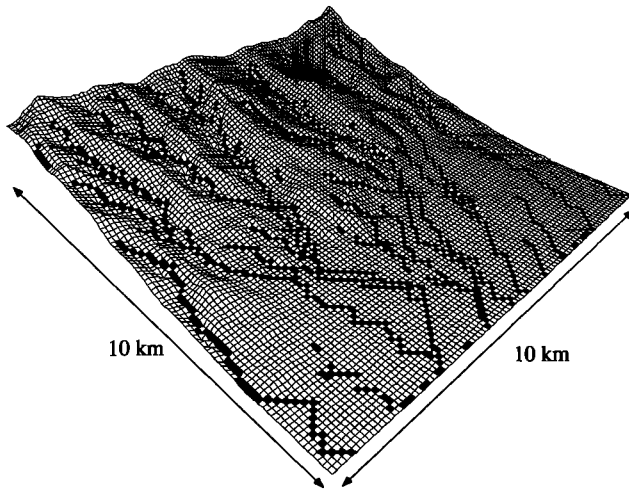


Figure 3. Topography from the Humboldt Range, Nevada, from USGS 3-arcsec DEM data, and the synthetic channel network generated on that topography by ZSCAPE. Nodes designated as channels by ZSCAPE are shown in black. The extent and interconnectedness of the channel network are directly dependent on the threshold channel power Ω_0 used in the experiment (Table 1).

a portion of the hillslope. This resulted in a commonly observed inner gorge that was removed only by the largest slides.

We therefore select potential sites of landslide initiation, or targets, as the lowest points on each hillslope whose topographic gradient exceeds a critical material friction angle ϕ (Figure 3). This ensures that landslides begin near the toe of hillslopes and that they initiate only on hillslopes that are steep enough to promote failure.

Hillslope failure may be caused by a number of events, including intense precipitation or coseismic shaking, weathering and subsequent weakening of planes within the rock mass, or a fall in local base level. Here we simply consider landslides caused by base level fall. We expect that as base level falls, the hillslope toe will become steeper and less buttressed, and thus more likely to fail. To assess the local potential for failure, we employ the Culmann slope stability criterion [Spangler and Handy, 1982], which holds that the maximum stable height that a hillslope may attain will be reached when the shear stress on a potential failure plane within the hillslope is balanced by the shear strength on that plane. In terms of forces, the effective weight of the hillslope material is

$$F_{\text{eff}} = F_w \sin \theta \quad (10)$$

where F_w is the weight of the hillslope material and θ is the dip of the potential failure plane. The balancing shear resistance is given by

$$F_r = CL + F_w \cos \theta \tan \phi \quad (11)$$

where C is the effective cohesion on the plane, L is the length of the failure plane, and ϕ is the effective friction angle on the plane [Spangler and Handy, 1982]. At the edge of stability, $F_{\text{eff}} = F_r$, and failure will occur at a critical angle θ_c that maximizes the effective cohesion on the failure plane, which may be expressed as

$$C = \frac{1}{2} \rho g H \frac{\sin(\beta - \theta) \sin(\theta - \phi)}{\sin(\beta) \cos(\phi)} \quad (12)$$

where ρ is rock density, g is gravitational acceleration, β is surface slope, and H is the hillslope height. The derivative of C with respect to θ is

$$\frac{\partial C}{\partial \theta} = \frac{1}{2} \rho g H \frac{\sin(\beta - 2\theta + \phi)}{\sin(\beta) \cos(\phi)} \quad (13)$$

so that C is maximized at $\theta_c = 1/2(\beta + \phi)$. Substituting θ_c in (12) and solving for H provides the maximum stable height of the hillslope H_c :

$$H_c = \frac{4C}{\rho g} \frac{\sin \beta \cos \phi}{[1 - \cos(\beta - \phi)]} \quad (14)$$

Since by definition the hillslope height H is always less than or equal to H_c , we can calculate a probability of failure

$$P_{\text{fail}} = \frac{H}{H_c} \quad (15)$$

that varies between 0 and 1 (Figure 4). We take the true failure probability to be the base probability plus a term that increases linearly through time at a rate dictated by the time since the last landslide at that node. This crudely accounts for time-dependent weakening of the failure plane and rock mass.

The potential size of a bedrock landslide is a function of local topography and relief, topographic gradient, rock strength, and the distribution, orientation, and strength of potential failure planes. We again employ the Culmann criterion, which predicts that the most likely failure plane is one that passes through the toe of the slope and dips at θ_c .

A potential failure plane, dipping at θ_c , is assumed to daylight at every potential landslide target (Figure 4). We project that failure plane outward and upward to all neighboring nodes within a specified distance from the target. The latter condition prevents, for example, nodes on the other side of a stream channel from failing. Those nodes whose surface elevation is above the projected failure plane are considered unstable, and the volume of material between the surface and the failure plane is recorded. The maximum potential landslide size at each target is the sum of the volumes at all unstable nodes associated with that target.

During each time step, the failure probability at each land-

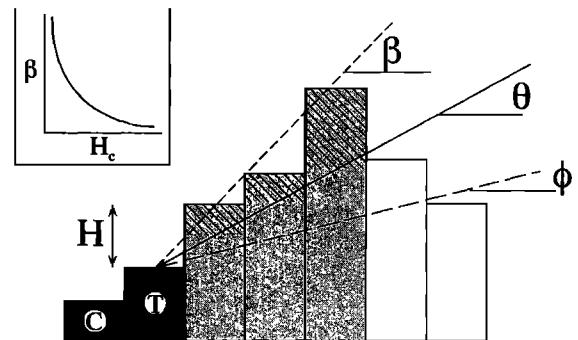


Figure 4. Schematic diagram of the bedrock landsliding algorithm. A landslide target (marked "T") is assigned as the lowest point above the channel (marked "C") at which $\beta > \phi$. The potential failure plane dips at θ and is assumed to be exposed at the target. The probability of failure is given by the ratio of the local hillslope height H to the maximum stable hillslope height H_c , which in turn depends upon the rock strength and the topographic gradient (inset).

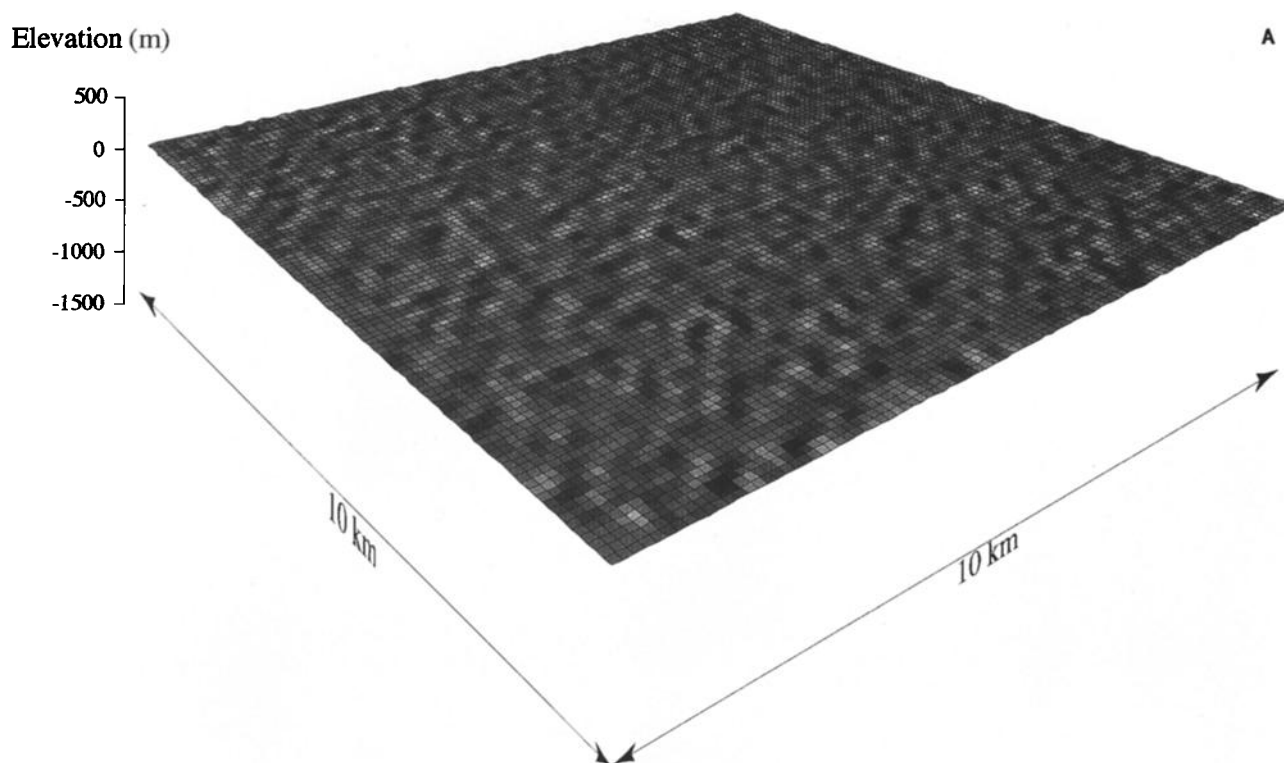


Figure 5. Shaded relief perspective views of surface topography from experiment 1 after (a) 0, (b) 500, and (c) 1000 kyr. All plots in this and subsequent plates are 10 km by 10 km, and vertical exaggeration is 2 \times .

slide target is compared with a uniform deviate. If the uniform deviate is smaller than the failure probability, a landslide initiates at that node. The size of the landslide is directly proportional to the time since the last landslide at that node. This is motivated by the observation that the size of slides in a physical hillslope model is primarily a function of the time since the last event [Densmore *et al.*, 1997]. The size is limited by the maximum potential size determined above.

After failure, the depositional pattern of the failed material depends strongly on both its rheology and the topography of the runout path. Thus a rockfall behaving as a Coulomb material may form a steep talus, while a more fluid, viscous debris flow may form a deposit with a much lower surface slope and considerably longer runout. The present algorithm spreads the resulting volume of material down the path of steepest descent as a deposit three nodes wide. We specify both the longitudinal (2°) and the lateral (5°) surface slopes of the deposit, which results in a debris flowlike tongue of failed material. The material is deposited as regolith, meaning it may subsequently be remobilized by other geomorphic processes.

5. Experimental Results

We first describe the synthetic landscapes generated by ZSCAPE, both with and without the bedrock landsliding rule enabled, and compare those landscapes with selected examples of mountainous topography from the Basin and Range province using simple statistical measures. We quantify the role of bedrock landslides by examining the model erosion rates due to different geomorphic processes. We then explore the responses of both the hillslope and fluvial systems to changes in tectonic activity and precipitation. Finally, we examine the

spatial and temporal distribution of landslides predicted by ZSCAPE and compare them with distributions from real landscapes.

We compare our results with topography from ranges that are bounded by active normal faults and that show clear signs of tectonic activity, such as linear range fronts, triangular facets, and piedmont fault scarps [Wallace, 1978]. On the basis of our field observations and the work of Stewart [1980] and Wallace [1978], among others, we identify five ranges in particular that meet our criteria: the Humboldt, Stillwater, Tobin, and Toiyabe Ranges in Nevada, and Steens Mountain in Oregon. We emphasize that while our synthetic landscapes are compared below with specific ranges, the visual and statistical signatures of these ranges are very similar despite their widely disparate tectonic and lithologic histories. We draw comparisons with a variety of ranges in order to highlight the consistent form taken by these active-fault-bounded mountains.

It is worth noting that the few existing data on landslide occurrence and magnitude-frequency distributions come from high-relief regions with high tectonic deformation rates, such as the Andes [Blodgett *et al.*, 1996] and the Southern Alps of New Zealand [Hovius *et al.*, 1997]. No such data have been collected for mountains of the Basin and Range. We therefore rely on the topography of these ranges, which after all is due to the integrated effect of geomorphic and tectonic processes, to constrain our present set of experiments.

5.1. Synthetic and Real Landscapes

In experiment 1 we begin with a gently tilted (1°) initial surface on which there is up to 5 m of randomly distributed bedrock topography, and up to 1 m of randomly distributed regolith (Figure 5a). We track the topography through 1000

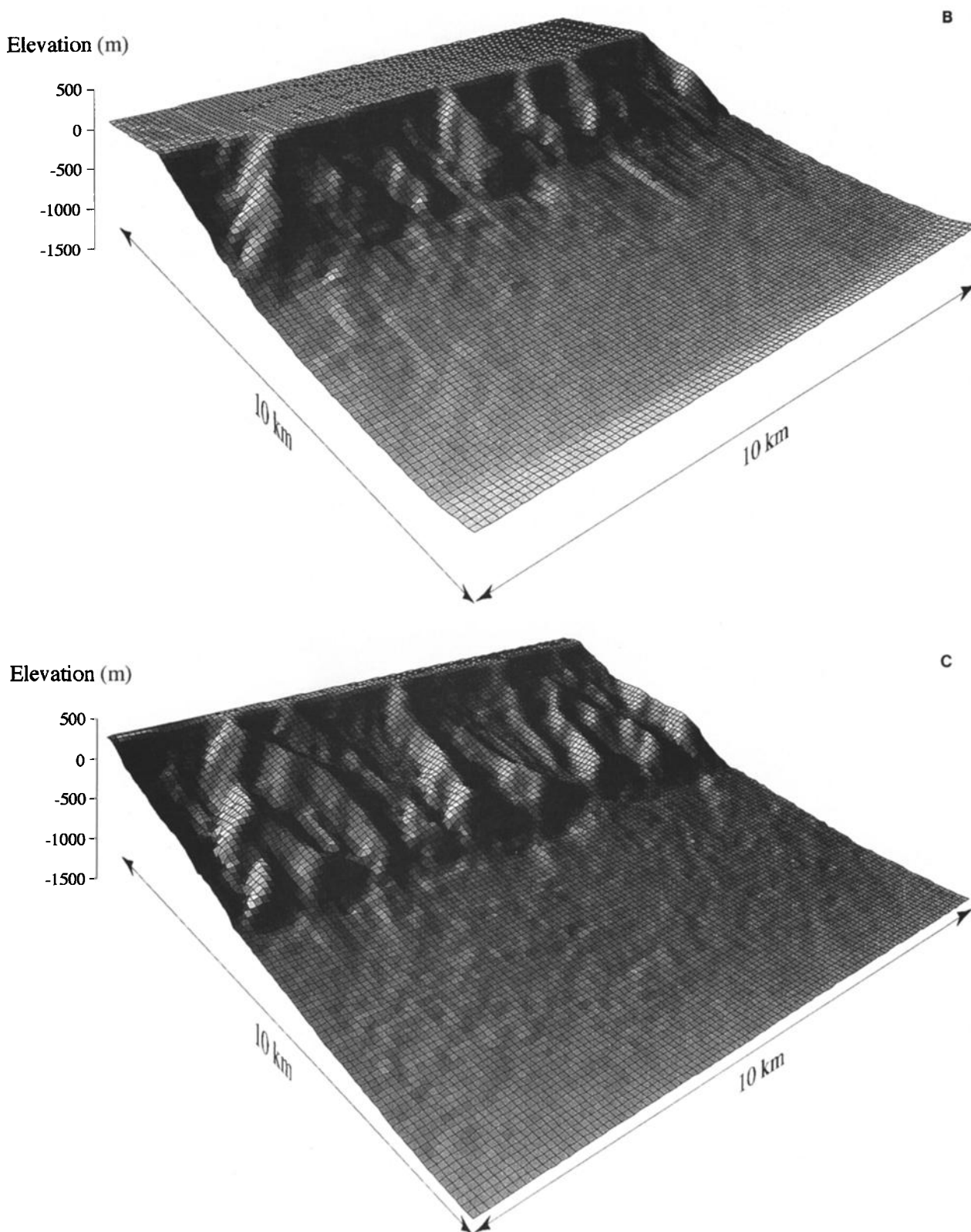


Figure 5. (continued)

kyr of model run time, with all tectonic and geomorphic processes active. The resulting landscape (Figures 5b and 5c) appears remarkably similar to topography from many normal-fault-bounded mountain ranges, such as the Stillwater and Toiyabe Ranges in Nevada (Figure 6). The landscape contains

a number of characteristic landforms that are observed along active normal-fault-bounded ranges [Wallace, 1978]. Catchments within the mountain mass generally are short and steep and trend normal to the mountain front. The catchments are shaped somewhat like a wineglass, with a large collection area

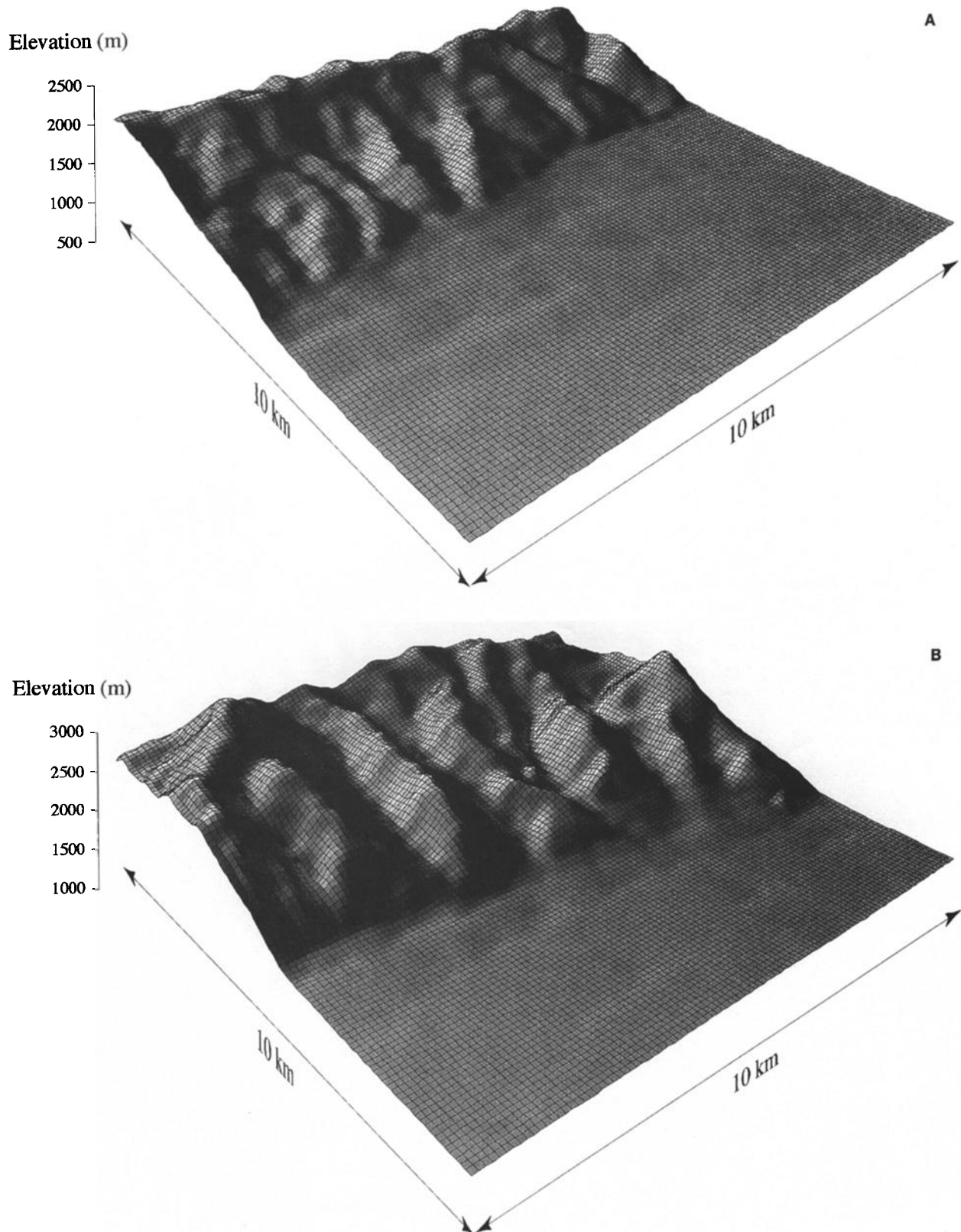


Figure 6. Shaded relief perspective views of (a) part of the east face of the Stillwater Range, Nevada, and (b) part of the east face of the Toiyabe Range, Nevada, from USGS 3-arcsec DEM data.

and a narrow canyon at the mountain front [Wallace, 1978]. The spurs between the catchments are truncated, forming triangular facets [Davis, 1903; Hamblin, 1976]. Finally, material removed from the catchments is deposited very close to the

mountain front within a hanging-wall basin. These deposits, which are fanlike at first, eventually coalesce to form a bajada on the hanging-wall block.

The role of landsliding in the evolution of these mountain

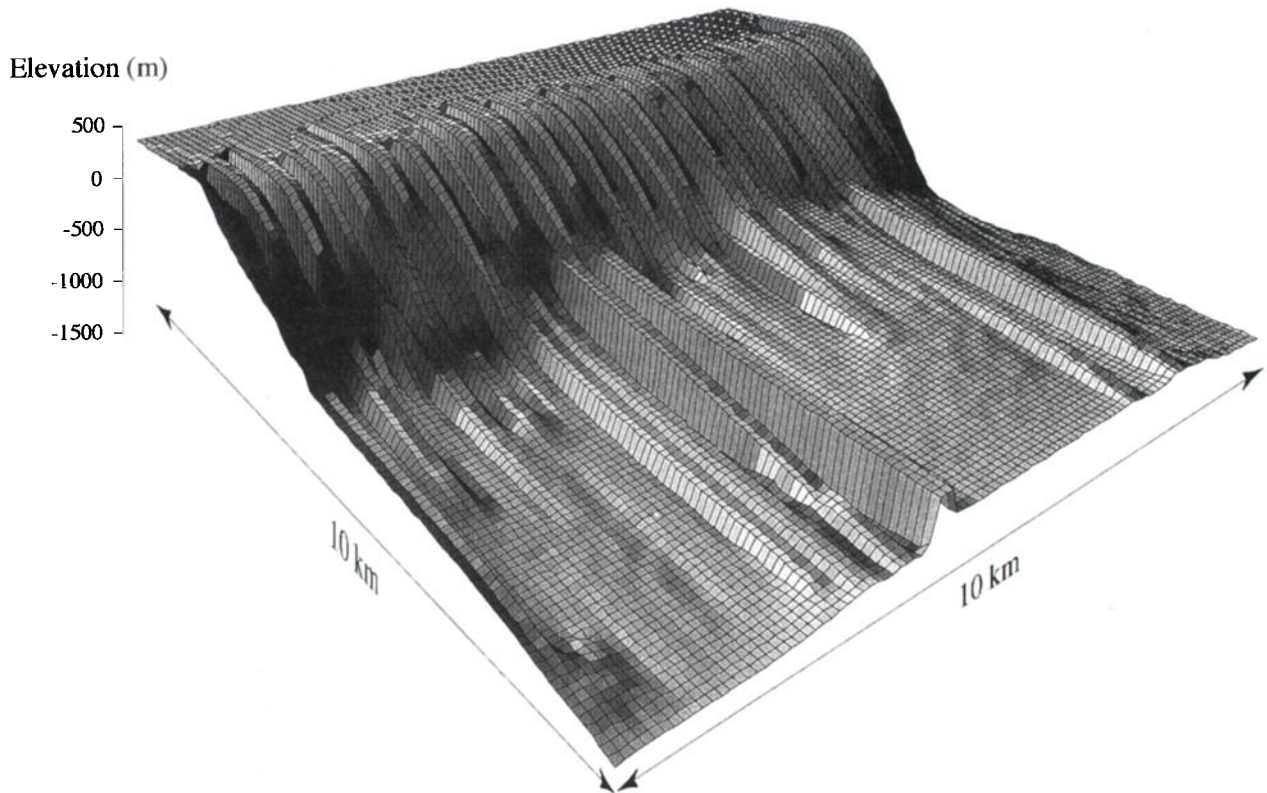


Figure 7. Shaded relief perspective view of topography after 1000 kyr from experiment 2. In this experiment, landsliding is disabled, and hillslope evolution occurs solely by regolith production and weathering-limited diffusion.

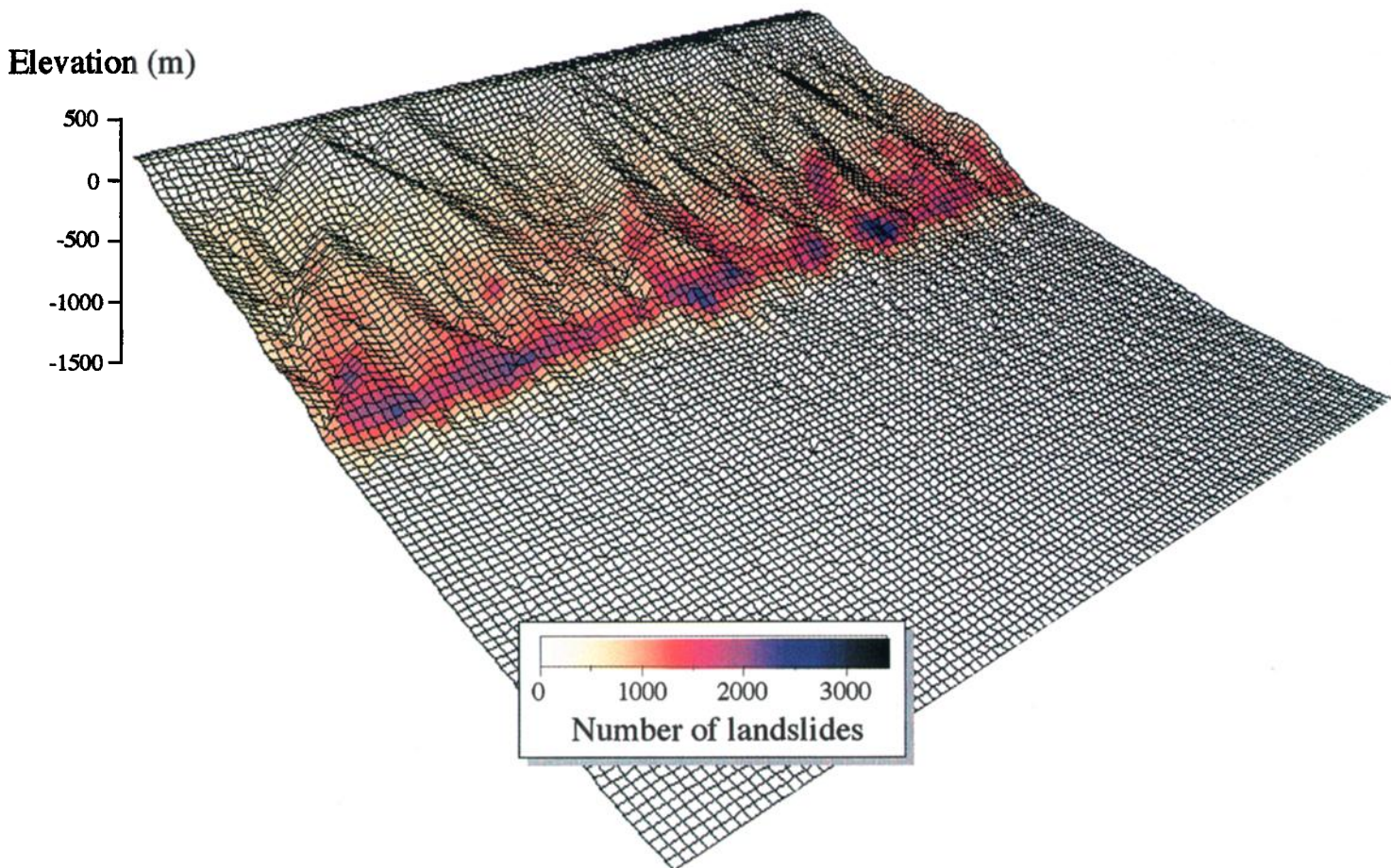


Plate 1. Shaded perspective view of the topography from experiment 1. The shading indicates the number of landslides that have occurred at each node during the 1000-kyr model run.

fronts may be judged by comparing the results of experiment 1 (Figure 5c) with those of experiment 2, in which the landslide algorithm is turned off (Figure 6). In experiment 2 the hillslopes evolve only by regolith production and linear diffusion, and the catchments are unable to widen significantly. This results in considerably steeper hillslopes and a much higher drainage density than in experiment 1 (Figure 7). Drainage density, relief, and mean slope along a representative cross section across the footwall block of the Humboldt Range, Nevada, are far better reproduced by experiment 1 than by experiment 2 (Figure 8).

The probability distributions of elevation and of topographic slope indicate that experiment 1 is a better approximation of real topography than is experiment 2 (Figure 9). Distributions from the Tobin and Toiyabe Ranges, as well as from Steens Mountain in Oregon, appear remarkably consistent, despite wide variations in lithology and fault activity (Figure 9), indicating that the distributions are relatively insensitive to these parameters. Experiment 1 yields probability distributions of elevation and slope that are similar to those of the ranges. In contrast, experiment 2 yields very different distributions, which implies that weathering-limited diffusion alone is unable to statistically reproduce Basin and Range topography. As was stated above, other workers have circumvented this by folding mass movements into a transport-limited diffusion law and by resorting to artificially high values of diffusivity. We show below that by treating bedrock landsliding as a separate process, we gain additional insights into the effects of landsliding on topography.

5.2. Role of Bedrock Landsliding in Landscape Evolution

The effects of landsliding are highly dependent on the heterogeneity of slope distribution. As expected, the greatest

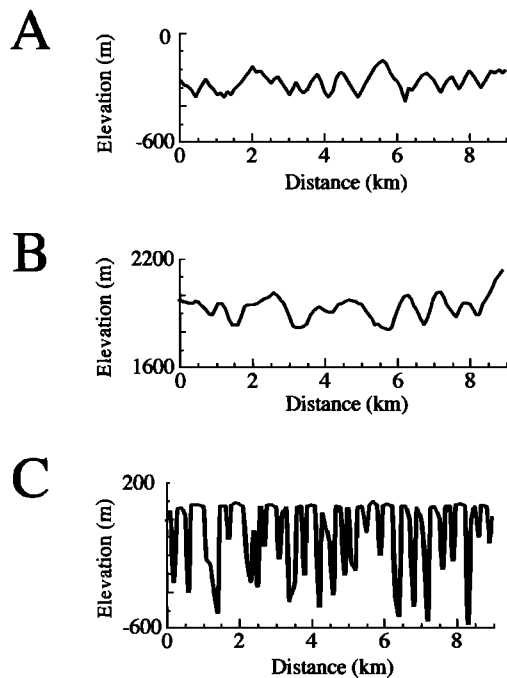


Figure 8. Cross sections, parallel to the strike of the range front, across the footwall block of (a) experiment 1, (b) the Humboldt Range, Nevada (taken from 3-arcsec DEM data), and (c) experiment 2. Vertical exaggeration is 5× for each profile.

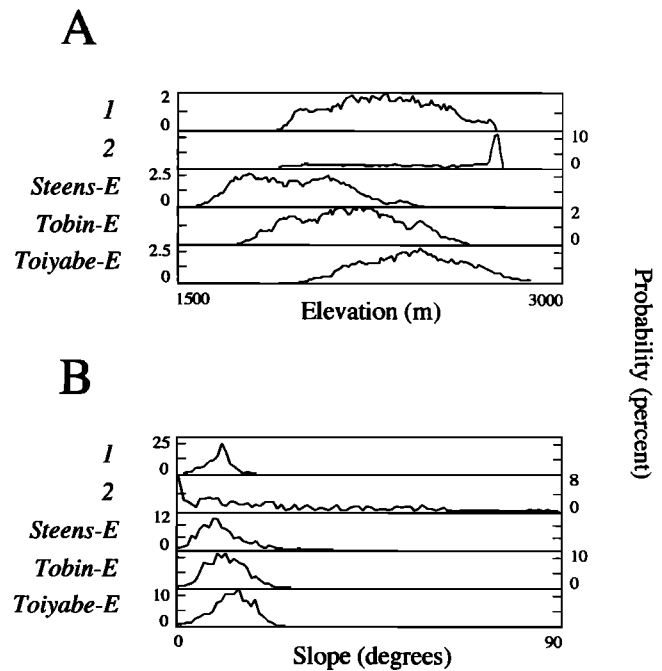


Figure 9. Probability distributions of (a) elevation and (b) slope, derived from the topography of experiments 1 and 2 and from 3-arcsec DEM data from the Tobin and Toiyabe Range, Nevada, and Steens Mountain, Oregon. These three normal-fault-bounded ranges yield compact, distinctly peaked distributions that appear very similar despite differences in lithology and tectonic history. Experiment 1 yields distributions much like those of the three ranges. In contrast, experiment 2 shows an excess of area at high elevations, as well as an excess of high slopes. These are due to an abundance of high, slowly diffusing interfluves and very steep catchment walls, respectively.

number of landslides in experiment 1 occur on the faceted spurs adjacent to the fault, and on the relatively long-lived hillslopes adjacent to the major channels (Plate 1). Hillslopes in the upper parts of the catchments, only recently excavated by channel incision, experience comparatively few landslides. An important corollary of this observation is that triangular facets are highly modified and shaped by geomorphic processes, and are therefore generally not simply exhumed remnants of the original fault surface.

In experiment 1, bedrock landsliding is the dominant erosional process on the footwall block, except within the bottoms of stream valleys (Figure 10). Initial sculpting of the footwall is by fluvial incision, which sets the conditions for subsequent hillslope development by landsliding. The efficient delivery of sediment to the valleys by landsliding causes continual change in the channel network, as channels migrate and adjust to the changing sediment load and slope distribution. This migration is manifested as relatively broad zones within the valleys in which fluvial erosion is the dominant process (Figure 10). Fluvial and bedrock landsliding processes yield long-term (1000 kyr), spatially and temporally averaged erosion rates of 0.8 and 0.5 mm yr⁻¹, respectively (Figure 11). In contrast, the mean rate of relief generation across the fault, given by the sum of the mean rates of uplift and subsidence, is 0.9 mm yr⁻¹. Fluvial and landsliding processes are by far the dominant geomorphic agents; the mean long-term regolith production rate during the

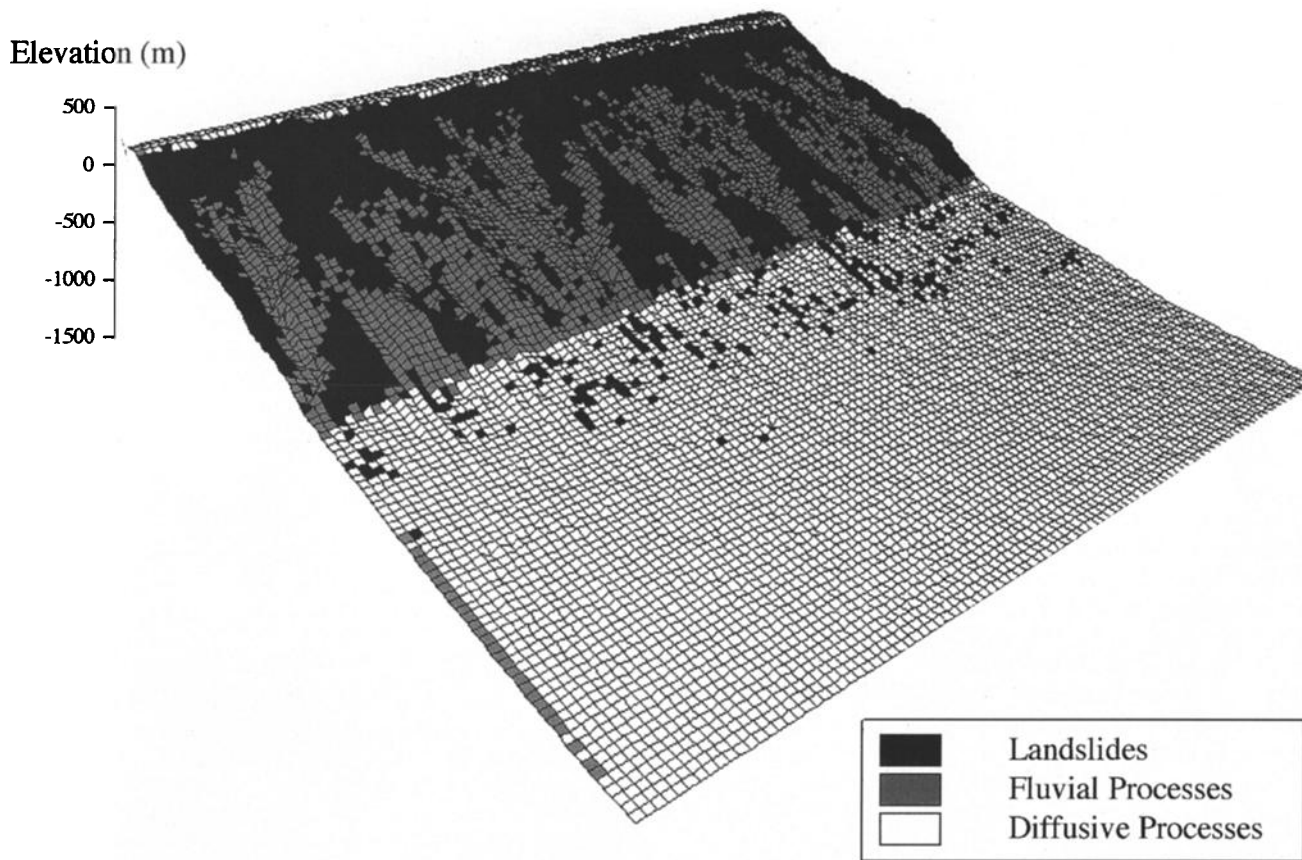


Figure 10. Shaded perspective view of the topography from experiment 1. The shading indicates which geomorphic process has resulted in the highest erosion rate at each node, averaged over the entire 1000-kyr run. Fluvial processes dominate the erosion of stream channels and some of the lower hillslopes, while landslides dominate on the upper hillslopes of the catchments and on the interfluves. Diffusion is only important on the largely depositional hangingwall block, and near the uppermost edge of the model space, where little stream power is available for channel incision.

run is 0.006 mm yr^{-1} , and the mean erosion rate due to regolith diffusion on hillslopes is 0.05 mm yr^{-1} (Figure 11).

Few data exist with which to compare these synthetic erosion rates. No landslide erosion rates in the Basin and Range prov-

ince have been published owing in part to the modern aridity and paucity of active landslides. Available landslide erosion rates and distributions are primarily from areas with high rates of precipitation and tectonic uplift [Kelsey, 1980; Pearce and

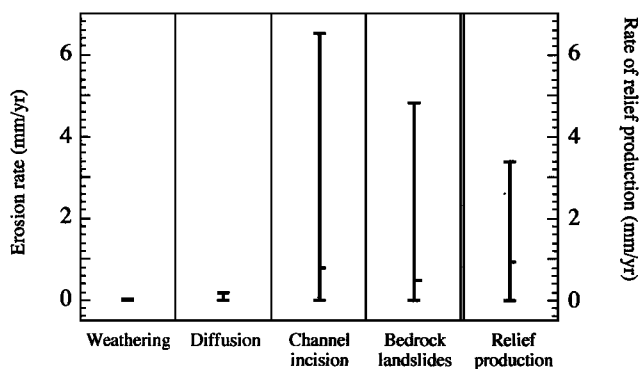


Figure 11. Long-term (averaged over 1000 kyr) erosion rates as a function of process in experiment 1. Vertical bars show the spatial variability in the erosion rates: half-width horizontal bars are the spatial mean rate. The rates are calculated by summing the erosion or surface lowering due to each process over the entire 1000-kyr model run. Note that weathering results in lowering of the bedrock elevation, rather than the surface elevation; it is included here for comparison.

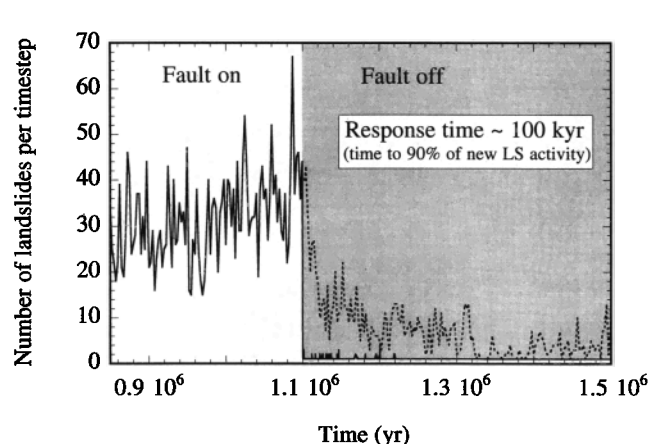


Figure 12. Time series of the number of landslides per time step, experiments 3 and 4. In experiment 3 (dashed line), fault activity ceases at 1100 kyr and precipitation is kept constant at 1.0 m yr^{-1} . In experiment 4 (solid line), fault activity ceases and precipitation falls from 1.0 m yr^{-1} to 0.1 m yr^{-1} at 1100 kyr.

Watson, 1986; Blodgett et al., 1996; Hovius et al., 1997]. Kelsey [1980] documented sediment fluxes consistent with a spatially averaged erosion rate of $\sim 1 \text{ mm yr}^{-1}$ in the Van Duzen River basin of northern California. He also found that debris slides in competent bedrock supplied a significant fraction of sediment to the channel system. Blodgett et al. [1996] inferred landslide erosion rates of $10\text{--}14 \text{ mm yr}^{-1}$ in the Bolivian Andes, significantly higher than long-term fission track denudation rates of $0.7\text{--}2.8 \text{ mm yr}^{-1}$. Hovius et al. [1997] calculated landslide erosion rates, averaged over 38 years, of $5\text{--}12 \text{ mm yr}^{-1}$ in catchments on South Island, New Zealand; these are rates consistent with measured fluvial sediment fluxes.

5.3. Landscape Response Time

Continuous landscape activity requires that the local hillslope base level be consistently lowered. In our experiments this is accomplished by (1) continued activity on the fault, which lowers both global base level for channels draining the footwall and local base level for hillslopes along the mountain front, and (2) continued precipitation, which provides the channels with enough stream power to incise. We can assess the importance of these factors in landslide generation by abruptly changing one or both during a model run. In experiment 3, precipitation is held constant at 1.0 m yr^{-1} throughout the run, but activity on the fault stops at 1100 kyr of model run time (Figure 12). The number of landslides per time step decays rapidly, reaching 90% of the new mean in $\sim 100 \text{ kyr}$ (Figure 12).

This 100-kyr response time may be thought of as a convolution of two components: a fluvial component, during which channel incision is progressively replaced by aggradation throughout the network, and a hillslope component, during which landslides occur on unstable but previously unfailed hillslopes. The relative importance of these components may be estimated by comparing experiment 3 with experiment 4, in which precipitation is lowered by an order of magnitude to 0.1 m yr^{-1} , simultaneous with the cessation of fault activity. The landscape response time should thus reflect only the influence of the hillslope component, since all channel incision effectively ceases immediately. In fact, the number of landslides immediately decreases to ~ 0 per time step (Figure 12), indicating that the hillslope response time is extremely rapid compared with the fluvial response time. Thus, relative to the channels, the hillslopes rapidly achieve a steady state, as was assumed by Anderson [1994].

5.4. Landslide Statistics

Landslides in our experiments show significant variation in size with time (Figure 13a). The probability distribution of landslide size may be approximated by a power law, a behavior that is observed in laboratory landslide experiments [e.g., Grumbacher et al., 1993; Frette et al., 1996] as well as in natural settings [Noever, 1993; Blodgett et al., 1996; Hovius et al., 1997]. For experiment 1 we calculate a power law exponent of -2.2 , very similar to the exponents often observed in laboratory experiments (Figure 13c) [Frette et al., 1996]. In contrast, the few measured natural landslide distributions have yielded power law exponents of approximately -1.3 (Figure 13c) [Blodgett et al., 1996; Hovius et al., 1997]. One possible reason for this discrepancy lies in the differing spatial resolution of the methods used to observe landslide distributions. For example, Hovius et al. [1997] use repeat aerial photographs to assess the extent of landslides, and claim an areal resolution of $10^2\text{--}10^6$

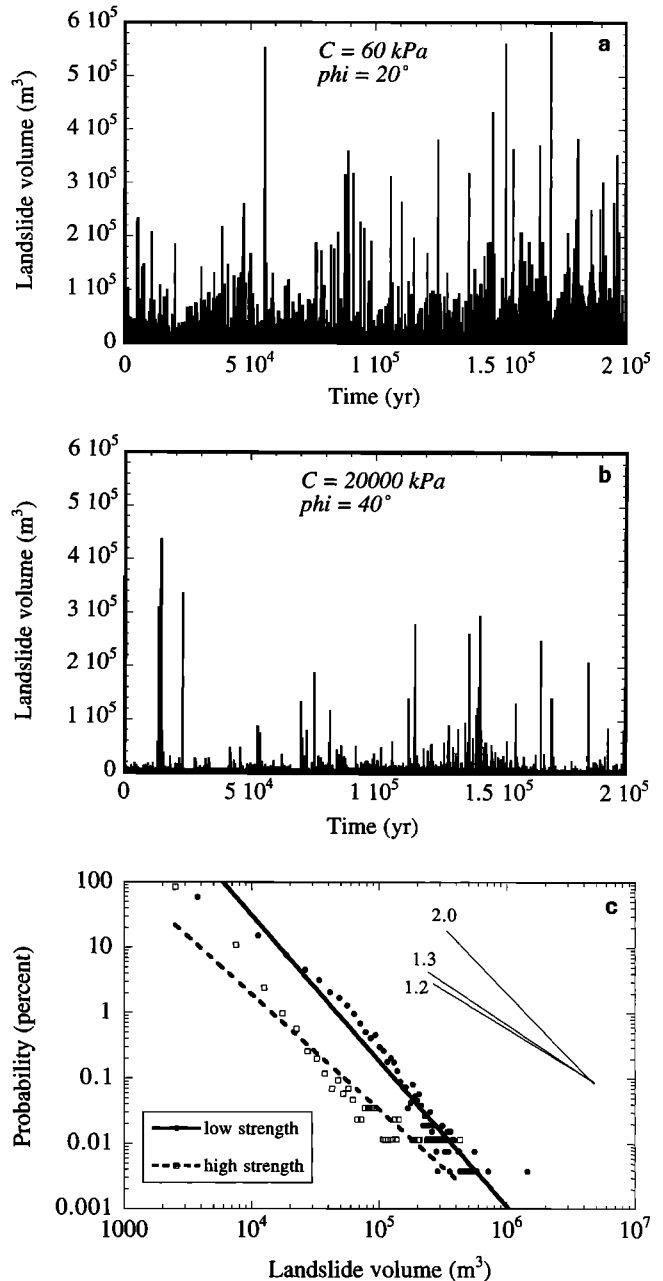


Figure 13. Time series and probability distributions of landslide sizes. (a) Time series of individual landslide volumes from experiment 1. Rock strength parameters are set to landscape-scale values derived by Schmidt and Montgomery [1995] for sedimentary rocks in the Santa Cruz Mountains, California. (b) Same as Figure 13a except that the strength parameters are set to laboratory-measured values presented by Schmidt and Montgomery [1995]. The high rock strength suppresses the number and volume of individual landslides. (c) Probability distributions of landslide volumes derived from the time series shown in Figures 13a and 13b. The low-strength distribution may be fit by a power law with exponent -2.2 , while the high-strength distribution is better fit by a power law exponent of -1.8 . The thin solid lines show schematically the exponents derived from natural (-1.3 [Blodgett et al., 1996] and -1.2 [Hovius et al., 1997]) and laboratory (-2.0 [Frette et al., 1996]) landslide distributions.

m². Our algorithm is limited to resolving landslides between 10⁴ and 2.5 × 10⁵ m² in area, which means that we may be unable to accurately reproduce portions of the landslide size spectrum in particular regions. Another potential reason for the difference in power law exponents is that the remote-sensing studies of *Blodgett et al.* [1996] and *Hovius et al.* [1997] compute landslide magnitude-frequency relations on the basis of landslide area, whereas we use landslide volume. *Hovius et al.* [1997] relate area to volume via an empirical function that may well be location-specific and may account for the variation in exponents.

The bedrock landsliding algorithm is primarily controlled by the rock cohesion and friction angle, which are complex, often time-dependent properties of the rock mass [Selby, 1993]. Values of these parameters for various rock types, measured both in the field and in the laboratory, range over several orders of magnitude [Schmidt and Montgomery, 1995]. Several workers [Selby, 1980; Schmidt and Montgomery, 1995] have pointed out that rock mass strength decreases with increasing spatial length scale. The appropriate rock strength values in ZSCAPE should therefore reflect the influence of discontinuities within the rock mass, rather than laboratory strength measurements. The majority of our experiments use landscape-scale values of cohesion and friction angle, $C = 60$ kPa and $\phi = 20^\circ$ (Santa Cruz Mountain sedimentary rock of Schmidt and Montgomery [1995]). The effect of rock strength on experimental landscapes is illustrated by experiment 5, in which we use values more typical of those measured in the laboratory, $C = 20,000$ kPa and $\phi = 40^\circ$ (hard sedimentary rock of Schmidt and Montgomery [1995]). The higher strength leads to steeper critical hillslope heights (equation (14)) and thus results in fewer and smaller landslides (Figure 13b). In addition, the smaller exponent implies that large landslides are relatively more abundant than in the low-strength experiments. However, we stress that experiments with nearly any degree of landsliding result in topography that is fundamentally different from that generated by weathering-limited diffusion alone.

6. Discussion

6.1. Fluvial Incision as a Rate-Limiting Process

The similarity between rates of erosion from fluvial and landslide processes implies that they are tightly coupled. This coupling is a natural consequence of their relative efficiency and response times and is not explicitly specified in the model. If landslides in a particular landscape are caused primarily by fluvial channel incision, as is modeled here, the degree of coupling will be quite high. However, if other mechanisms of destabilizing slopes, such as groundwater sapping or seismic accelerations, are present, we expect the coupling to be much less pronounced, as landsliding will occur in response to those other mechanisms as well.

In our experiments the rate of fluvial channel incision determines the rate at which the landscape evolves; the channel network sets the lengths and distribution of hillslopes and thus is primarily responsible for the gross morphology of the landscape. We argue therefore that field measurements of rates of landscape evolution in setting similar to our experiments should focus on rates of fluvial processes. Nevertheless, the stochastic nature of the landsliding process and its intrinsic response time can yield hillslopes that in essence lag behind the process of local base level lowering. This lag time may yield unstable hillslopes such as inner gorges that exist for relatively

long time periods ($\geq 10^3$ years). Inner gorges are commonly observed in actively eroding landscapes and may be misinterpreted as an indication of a recent increase in incision rate caused by regional base level lowering or climate change [Densmore et al., 1997].

Weissel and Seidl [1997] have shown that hillslope processes, particularly bedrock mass wasting, limit the headward propagation rate of drainages on the passive eastern margin of Australia. Their findings do not contradict our conclusions in this paper, as they deal with different stages of drainage basin evolution. Weissel and Seidl [1997] were concerned with the initial incision of a drainage network into low-relief topography, while our results apply to portions of the drainage network that have evolved to a steady state form and relief.

6.2. System Response as a Measure of Landscape Evolution

Kooi and Beaumont [1996] presented an analysis of landscape response times and the effects of the interaction between response time and timescales of tectonic forcing. They demonstrated quasi-linear behavior of their LEM, as evidenced by the exponential response of particular variables to step changes in tectonic forcing. We observe similar quasi-linear behavior in the evolution of our channel network. For example, the mean denudation rate on the footwall increases as $[1 - \exp(-t/t_*)]$ after a step increase in tectonic activity, where the timescale $t_* \approx 200$ kyr.

The bedrock landsliding algorithm also exhibits a characteristic response time after changes in tectonic activity, although the response is highly nonlinear. This is not surprising, given the nonlinear relationship between failure probability and hillslope gradient (equations (14) and (15)). Recall that an abrupt cessation of tectonic activity, and thus base level fall, causes a decrease in the number of landslides per time step, with a response time of the order of 100 kyr (Figure 12). We interpret this response time as reflecting the progressive cessation of channel incision and the onset of aggradation throughout the network. An initial wave of aggradation passes very rapidly up the network (on a timescale of < 10 kyr, which agrees with the observation of Wallace [1978] in the Basin and Range) and results in the precipitous initial drop in the number of landslides. Aggradation lowers hillslope heights, essentially freezing the failure probability at any particular target. Those hillslopes that are already steep enough to fail, do so eventually, and the lack of continued base level fall means that few new landslide-prone hillslopes are created.

6.3. Assumptions and Improvements

Our approach to modeling mass movements via landslides involves two algorithms, one for determining the location and size of a landslide and a second for distributing the failed material downslope. The first of these is motivated strongly by the physics and observations of slope failure both in the real world and in controlled experiments, although at present we ignore most of the range of landslide rheologies [e.g., Varnes, 1978]. The means of distributing failed material, however, is tied less to physics than to basic field observations. This is partly because the physics of slide material is strongly dependent on the rheology of the material. Our simple algorithm to distribute slide material can be tuned by adjusting a limited number of parameters, but we hasten to point out that these parameters are simple proxies for a complicated physical process. Particular applications of the model must at least involve

a landslide rule set that is modified to fit the dominant landslide type observed in the region.

We also ignore tectonic and climatic variations as potential landslide triggers. Seismic triggering of landslides is well documented [Keefer, 1984, 1994], and attempts have been made to relate earthquake magnitude to landslide likelihood [Wilson and Keefer, 1985; Jibson and Keefer, 1993]. There is disagreement, however, between theoretical and measured ground accelerations during earthquakes, primarily due to topographic effects [e.g., Geli *et al.*, 1988], and no general, physically based model of seismically triggered landsliding has yet been proposed.

Variations in climate should affect the bedrock landsliding algorithm in both direct and indirect ways, although we have not yet explored the effect of climate change on landscape development. In particular, we expect that increased precipitation should increase the channel incision rate and thus more rapidly lower the local base level seen by the hillslopes. In addition, higher precipitation will increase the rate at which information on ultimate base level (as dictated, for example, by tectonic activity) is transmitted upstream. More rainfall should also increase the regolith production rate and should result in saturation of the hillslope regolith, which would be reflected in a higher diffusivity and increased mass fluxes by regolith mass movement. Finally, increased precipitation will hasten weathering of the bedrock along joint planes, thereby decreasing the bulk cohesion and enabling bedrock landslides.

We approximate the accumulating tectonic displacement field by superposing displacement fields calculated from the initial flat surface rather than from the incrementally deforming surface. This leads to a progressively larger mismatch between the theoretical and applied displacement fields. This is a small source of error, however, since vertical gradients in the relief across the displacement field are of the order of 2.5% per kilometer of fault displacement. In experiment 1, for instance, total fault displacement is 3.3 km, implying an error of less than 10%.

ZSCAPE does not yet account for the flexural effects of differential loading and unloading, which have been shown to be significant in generating footwall uplift in an extensional setting [Weissel and Karner, 1989; King and Ellis, 1990]. We may obtain a crude estimate of the magnitude of the elevation changes due to flexure by calculating the displacement in response to the total load accumulated during an experiment. The negative load due to erosion is represented by the difference between the summed tectonic displacement envelope and the final bedrock topography, while the positive load due to deposition is simply the accumulated regolith thickness. Assuming an effective elastic thickness of 2 km [King and Ellis, 1990], differential elevation changes due to the flexural response to this load are ~80 m across the 10-km-wide space of experiment 1. In contrast, the cumulative tectonic relief across this same distance in experiment 1 is 620 m. This analysis is of course approximate, as it ignores the feedback between the flexural response and geomorphic activity [King and Ellis, 1990; Small and Anderson, 1995].

A final issue concerns the spatial resolution of the geomorphic rule set, particularly of the bedrock landsliding algorithm. Selby [1980], among others, helped to quantify the role played by joints and fractures in dictating rock strength and slope stability. Recent work by Weissel and Seidl [1997] has highlighted the dramatic effect that fracture density and orientation have on hillslope morphology. Such fine-scale variables

are at present ignored by the bedrock landsliding algorithm in ZSCAPE, being folded into the rock strength parameters. However, any analysis of the spatially distributed effects of fractures on hillslope morphology and landslide occurrence, as well as explicit comparisons between observed and synthetic landslide morphologies, will require an algorithm capable of resolving such variables.

As such issues are resolved, we believe that models such as ZSCAPE may eventually be useful in predicting the geomorphic evolution of specific sites. Accurate, high-resolution DEM data will serve as the template on which geomorphic and tectonic processes act; ZSCAPE is then ideally suited to monitor the evolution of topography, as well as landslide location and size, erosion rates, and sediment fluxes. Such simulations will provide an independent, long-term check on historically measured parameters such as catchment sediment fluxes, and may help to determine whether modern process rate measurements agree with long-term equilibria.

7. Conclusions

We have demonstrated the first quantitative model of landscape evolution that includes a realistic tectonic deformation input and erosion by bedrock landslides, and have shown that it produces landscapes that are consistent with laboratory and field observations. In particular, we draw the following conclusions:

1. Our experiments support the hypothesis that bedrock landsliding is an important process in the evolution of realistic mountainous topography. A weathering-limited diffusion rule, although appropriate for modeling regolith transport in many environments, cannot remove sufficient material from the model space using field-measured values of topographic diffusivity. While previous studies have simulated bedrock landsliding by using artificially high diffusivities, we argue that such approaches obscure the contribution of discrete, large landslide events to landscape development.

2. Experimental rates of erosion due to bedrock landsliding are comparable to those due to fluvial channel incision. In addition, the response time of individual hillslopes to changes in local baselevel is very rapid compared with the response time of the channel network as a whole. These lines of evidence argue that fluvial and landsliding processes are tightly coupled. In steady state, and in the absence of alternative means of generating landslides (such as groundwater sapping or seismic accelerations), fluvial channel incision is the rate-limiting process of landscape evolution. Bedrock landslides allow the hillslopes to keep pace with channel incision.

3. Rates of bedrock landsliding respond nonlinearly to temporal changes in tectonic activity. On the basis of the rapid hillslope response, we attribute the bedrock landslide response time to progressive aggradation and adjustment of the channel network.

4. A simple, stochastic bedrock landsliding algorithm is sufficient to generate landslide size distributions that show power law behavior, consistent with laboratory experiments. There is some discrepancy between numerically derived and field-measured exponent values, which may be due to differences in spatial resolution between the numerical model and remote-sensing measurement techniques, or to differences between volume-frequency and area-frequency relationships.

Finally, we wish to point out the need for additional data on landslide size distributions and temporal sequences from a

variety of geologic environments. In particular, we stress that future field investigations should focus on fluvial and bedrock landsliding processes, as our experiments demonstrate that these are responsible for the bulk of the geomorphic work done on the landscape.

Notation

A	drainage area, m^2 .
β	topographic slope, rad.
β_{crit}	critical topographic slope for shallow landsliding, rad.
C	cohesion, $kg\ m^{-1}\ s^{-2}$.
C_r	runoff coefficient, dimensionless.
Δt	timestep, years.
Δx	grid spacing, m.
F_{eff}	component of weight of hillslope material along failure plane, $kg\ m\ s^{-2}$.
F_w	weight of hillslope material, $kg\ m\ s^{-2}$.
F_r	resisting force along failure plane, $kg\ m\ s^{-2}$.
g	gravitational acceleration, $m\ s^{-2}$.
γ	unit weight, $kg\ m^{-2}\ s^{-2}$.
H	hillslope height, m.
H_c	maximum hillslope height, m.
k	diffusion coefficient, $kg\ m^{-1}\ s^{-1}$.
κ	diffusivity, $m^2\ s^{-1}$.
k_a	alluvial sediment transport coefficient, $m^2\ s^2\ kg^{-1}$.
k_b	bedrock incision coefficient, $m\ s^2\ kg^{-1}$.
k_w	channel width coefficient, dimensionless.
L	hillslope length, m.
Ω	stream power per unit bed width, $kg\ s^{-3}$.
Ω_0	threshold stream power per unit bed width, $kg\ s^{-3}$.
Ω_{excess}	excess stream power per unit bed width, $kg\ s^{-3}$.
p_{fail}	probability of failure, dimensionless.
P	precipitation rate, $m\ s^{-1}$.
ρ	bulk density, $kg\ m^{-3}$.
ϕ	material friction angle, rad.
q_s	mass transport per unit width, $kg\ m^{-1}\ s^{-1}$.
Q_s	volumetric transport rate per unit width, $m^2\ s^{-1}$.
R	regolith thickness, m.
R_*	depth of maximum regolith production, m.
R_{scale}	regolith production lengthscale, m.
$\partial R/\partial t$	regolith production rate, $m\ yr^{-1}$.
$(\partial R/\partial t)_0$	surface regolith production rate, $m\ yr^{-1}$.
$(\partial R/\partial t)_*$	maximum regolith production rate, $m\ yr^{-1}$.
S	channel bed slope, rad.
τ_r	earthquake recurrence interval, years.
θ	failure plane dip, rad.
θ_c	critical angle of failure, deg.
w	channel width, m.
z	surface elevation, m.
z_b	bedrock surface elevation, m.

Acknowledgments. We thank Niels Hovius and Jeff Weissel for discussions, and Dorothy Merritts, Jeff Weissel, and Sean Willett for excellent reviews. Ed Boring provided valuable advice on the numerical modeling. Supported by a NASA Topography and Surface Change grant to M.A.E. and R.S.A. and by a NASA Earth System Science Graduate Fellowship to A.L.D. CERL contribution 317.

References

Ahnert, F., Brief description of a comprehensive three-dimensional process-response model of landform development, *Z. Geomorphol.*, 24, suppl., 11–22, 1970.

- Anderson, R. S., Evolution of the Santa Cruz Mountains, California, through tectonic growth and geomorphic decay, *J. Geophys. Res.*, 99, 20,161–20,179, 1994.
- Anderson, R. S., and N. F. Humphrey, Interaction of weathering and transport processes in the evolution of arid landscapes, in *Quantitative Dynamic Stratigraphy*, edited by T. A. Cross, pp. 349–361, Prentice Hall, Englewood Cliffs, N. J., 1989.
- Anderson, R. S., and K. M. Menking, The Quaternary marine terraces of Santa Cruz, California: Evidence for coseismic uplift on two faults, *Geol. Soc. Am. Bull.*, 106, 649–664, 1994.
- Bagnold, R. A., Bed load transport by natural rivers, *Water Resour. Res.*, 13, 303–312, 1977.
- Beaumont, C., H. Kooi, and S. Willett, Progress in coupling tectonic-surface process models with applications to rifted margins and collisional orogens, in *Geomorphology and Global Tectonics*, edited by M. A. Summerfield, in press, 1998.
- Bierman, P. R., Using in situ produced cosmogenic isotopes to estimate rates of landscape evolution: A review from the geomorphic perspective, *J. Geophys. Res.*, 99, 13,885–13,896, 1994.
- Blodgett, T. A., B. L. Isacks, E. J. Fielding, J. G. Masek, and A. S. Warner, Erosion attributed to landslides in the Cordillera Real, Bolivia (abstract), *Eos Trans. AGU*, 17(17), Spring Meet. Suppl., S261, 1996.
- Burbank, D. W., J. Leland, E. Fielding, R. S. Anderson, N. Brozovic, M. R. Reid, and C. Duncan, Bedrock incision, rock uplift and threshold hillslopes in the northwestern Himalayas, *Nature*, 379, 505–510, 1996.
- Costa, J. E., and J. E. O'Connor, Geomorphically effective floods, in *Natural and Anthropogenic Influences in Fluvial Geomorphology*, *Geophys. Monogr. Ser.*, vol. 89, edited by J. E. Costa et al., pp. 45–56, AGU, Washington, D. C., 1995.
- Costa, J. E., and R. L. Schuster, The formation and failure of natural dams, *Geol. Soc. Am. Bull.*, 100, 1054–1068, 1988.
- Crouch, S. L., and A. M. Starfield, *Boundary Element Methods in Solid Mechanics*, Allen and Unwin, Winchester, Mass., 1983.
- Davis, W. M., The mountain ranges of the Great Basin, *Bull. Mus. Comp. Zool., Harv. Coll.*, 42, 129–177, 1903.
- Densmore, A. L., R. S. Anderson, B. G. McAdoo, and M. A. Ellis, Hillslope evolution by bedrock landslides, *Science*, 275, 369–372, 1997.
- Dixon, T. H., S. Robaudo, J. Lee, and M. C. Reheis, Constraints on present-day Basin and Range deformation from space geodesy, *Tectonics*, 14(4), 755–772, 1995.
- Elliott, D., The energy balance and deformation mechanics of thrust sheets, *Philos. Trans. R. Soc. London, Ser. A*, 283, 289–312, 1976.
- Ellis, M. A., A. L. Densmore, and R. S. Anderson, Topography as a measure of regional strain: Results of a coupled tectonic-geomorphologic model (abstract), *Eos Trans. AGU*, 76(17), Spring Meet. Suppl., S278, 1995.
- Frette, V., K. Christensen, A. Malthe-Sørensen, J. Feder, T. Jøssang, and P. Meakin, Avalanche dynamics in a pile of rice, *Nature*, 379, 49–52, 1996.
- Geli, L., P.-Y. Bard, and B. Jullien, The effect of topography on earthquake ground motion: A review and new results, *Bull. Seismol. Soc. Am.*, 78, 42–63, 1988.
- Gibbons, A. B., J. D. Megeath, and K. L. Pierce, Probability of moraine survival in a succession of glacial advances, *Geology*, 12, 327–330, 1984.
- Gilbert, G. K., Studies of Basin-Range structure, *U.S. Geol. Surv. Prof. Pap.*, 153, 1928.
- Gilchrist, A. R., H. Kooi, and C. Beaumont, Post-Gondwana geomorphic evolution of southwestern Africa: Implications for the controls on landscape development from observations and numerical experiments, *J. Geophys. Res.*, 99, 12,211–12,228, 1994.
- Gomberg, J., and M. Ellis, 3D-DEF: A user's manual, *U.S. Geol. Surv. Open File Rep.*, 93–547, 1993.
- Gomberg, J., and M. Ellis, Topography and tectonics of the central New Madrid seismic zone: Results of numerical experiments using a three-dimensional boundary element program, *J. Geophys. Res.*, 99, 20,299–20,310, 1994.
- Grumbacher, S. K., et al., Self-organized criticality—An experiment with sandpiles, *Am. J. Phys.*, 61, 329–335, 1993.
- Hamblin, W. K., Patterns of displacement along the Wasatch fault, *Geology*, 4, 619–622, 1976.
- Hanks, T. C., R. C. Bucknam, K. R. Lajoie, and R. E. Wallace,

- Modification of wave-cut and faulting-controlled landforms, *J. Geophys. Res.*, **89**, 5771–5790, 1984.
- Harbor, J. M., Numerical modeling of the development of U-shaped valleys by glacial erosion, *Geol. Soc. Am. Bull.*, **104**, 1364–1375, 1992.
- Heimsath, A. M., W. E. Dietrich, K. Nishiizumi, and R. C. Finkel, Soil production and landscape equilibrium: Hillslope analysis using cosmogenic nuclides in northern California and coastal Oregon (abstract), *Eos Trans. AGU*, **77**(46), Fall Meet. Suppl., F245–F246, 1996.
- Hovius, N., C. P. Stark, and P. A. Allen, Sediment flux from a mountain belt derived by landslide mapping, *Geology*, **25**, 231–234, 1997.
- Howard, A. D., A detachment-limited model of drainage basin evolution, *Water Resour. Res.*, **30**, 2261–2285, 1994.
- Howard, A. D., W. E. Dietrich, and M. A. Seidl, Modeling fluvial erosion on regional to continental scales, *J. Geophys. Res.*, **99**, 13,971–13,986, 1994.
- Jibson, R. W., and D. K. Keefer, Analysis of the seismic origin of landslides: Examples from the New Madrid seismic zone, *Geol. Soc. Am. Bull.*, **105**, 521–536, 1993.
- Keefer, D. K., Landslides caused by earthquakes, *Geol. Soc. Am. Bull.*, **95**, 406–421, 1984.
- Keefer, D. K., The importance of earthquake-induced landslides to long-term slope erosion and slope-failure hazards in seismically active regions, *Geomorphology*, **10**, 265–284, 1994.
- Kelsey, H. M., A sediment budget and an analysis of geomorphic processes in the Van Duzen River basin, north coastal California, 1941–1975, *Geol. Soc. Am. Bull.*, **91**, Part 2, 1119–1216, 1980.
- Kelsey, H. M., Formation of inner gorges, *Catena*, **15**, 433–458, 1988.
- King, G. C. P., and M. A. Ellis, The origin of large local uplift in extensional regions, *Nature*, **348**, 689–693, 1990.
- King, G. C. P., R. S. Stein, and J. B. Rundle, The growth of geologic structures by repeated earthquakes, 1, Conceptual framework, *J. Geophys. Res.*, **93**, 13,307–13,318, 1988.
- Kirkby, M. J., General models of long-term slope evolution through mass movement, in *Slope Stability: Geotechnical Engineering and Geomorphology*, edited by M. G. Anderson and K. S. Richards, pp. 359–379, John Wiley, New York, 1987.
- Kooi, H., and C. Beaumont, Escarpment evolution on high-elevation rifted margins: Insights derived from a surface process model that combines diffusion, advection, and reaction, *J. Geophys. Res.*, **99**, 12,191–12,209, 1994.
- Kooi, H., and C. Beaumont, Large-scale geomorphology: Classical concepts reconciled and integrated with contemporary ideas via a surface processes model, *J. Geophys. Res.*, **101**, 3361–3386, 1996.
- Koons, P. O., The topographic evolution of collisional mountain belts: A numerical look at the Southern Alps, New Zealand, *Am. J. Sci.*, **289**, 1041–1069, 1989.
- Koons, P. O., Three-dimensional critical wedges: Tectonics and topography in oblique collisional orogens, *J. Geophys. Res.*, **99**, 12,301–12,315, 1994.
- Massonnet, D., M. Rossi, C. Carmona, F. Adragna, G. Peltzer, K. Feigl, and T. Rabaute, The displacement field of the Landers earthquake mapped by radar interferometry, *Nature*, **364**, 138–142, 1993.
- Megahan, W. F., N. F. Day, and T. M. Bliss, Landslide occurrence in the western and central Northern Rocky Mountain physiographic province in Idaho, in *Forest Soils and Land Use: Proceedings of the Fifth North American Forest Soils Conference*, edited by C. T. Youngberg, pp. 116–139, Colo. State Univ., Fort Collins, 1978.
- Merritts, D., and M. A. Ellis, Introduction to special section on tectonics and topography, *J. Geophys. Res.*, **99**, 12,135–12,141, 1994.
- Miller, D. J., and T. Dunne, Topographic perturbations of regional stresses and consequent bedrock fracturing, *J. Geophys. Res.*, **101**, 25,523–25,536, 1996.
- Noever, D. A., Himalayan sandpiles, *Phys. Rev. E*, **47**, 724–725, 1993.
- Okada, Y., Internal deformation due to shear and tensile faults in a half-space, *Bull. Seismol. Soc. Am.*, **82**, 1018–1040, 1992.
- Pearce, A. J., and A. J. Watson, Effects of earthquake-induced landslides on sediment budget and transport over a 50-yr period, *Geology*, **14**, 52–55, 1986.
- Rosenbloom, N. A., and R. S. Anderson, Hillslope and channel evolution in a marine terraced landscape, Santa Cruz, California, *J. Geophys. Res.*, **99**, 14,013–14,029, 1994.
- Savage, J. C., M. Lisowski, J. L. Svarc, and W. K. Gross, Strain accumulation across the central Nevada seismic zone, 1973–1994, *J. Geophys. Res.*, **100**, 20,257–20,269, 1995.
- Schmidt, K. M., and D. R. Montgomery, Limits to relief, *Science*, **270**, 617–620, 1995.
- Seidl, M. A., and W. E. Dietrich, The problem of channel incision into bedrock, *Catena Suppl.*, **23**, 101–124, 1992.
- Seidl, M. A., J. K. Weissel, and L. F. Pratson, The kinematics and pattern of escarpment retreat across the rifted continental margin of SE Australia, *Basin Res.*, **12**, 301–316, 1996.
- Selby, M. J., A rock mass strength classification for geomorphic purposes: With tests from Antarctica and New Zealand, *Z. Geomorphol.*, **24**, 31–51, 1980.
- Selby, M. J., *Hillslope Materials and Processes*, Oxford Univ. Press, New York, 1993.
- Sharp, R. P., Basin-Range structure of the Ruby–East Humboldt Range, northeastern Nevada, *Geol. Soc. Am. Bull.*, **50**, 881–920, 1939.
- Sharp, R. P., Geomorphology of the Ruby–East Humboldt Range, Nevada, *Geol. Soc. Am. Bull.*, **51**, 337–372, 1940.
- Small, E. E., and R. S. Anderson, Geomorphologically driven late Cenozoic rock uplift in the Sierra Nevada, California, *Science*, **270**, 277–280, 1995.
- Small, E. E., and R. S. Anderson, Erosion rates of Laramide summit surfaces: Implications for late Cenozoic increases in summit elevations (abstract), *Geol. Soc. Am. Abstr. Programs*, **28**, A515, 1996.
- Spangler, M. G., and R. L. Handy, *Soil Engineering*, Harper and Row, New York, 1982.
- Spaulding, W. G., Vegetation and climates of the last 4500 years in the vicinity of the Nevada Test Site, south-central Nevada, *U.S. Geol. Surv. Prof. Pap.*, **1329**, 1985.
- Stein, R. S., G. C. P. King, and J. Rundle, The growth of geologic structures by repeated earthquakes, 2, Field examples of continental dip-slip faults, *J. Geophys. Res.*, **93**, 13,319–13,331, 1988.
- Stewart, J. H., Geology of Nevada: A discussion to accompany the Geologic Map of Nevada, *Spec. Publ. Nev. Bur. Mines Geol.*, **4**, 1980.
- Stock, J. D., and D. R. Montgomery, Can we predict the rate of bedrock river incision using the stream power law? (abstract), *Eos Trans. AGU*, **76**(46), Fall Meet. Suppl., F277, 1995.
- Suppe, J., Mechanics of mountain-building and metamorphism in Taiwan, *Mem. Geol. Soc. China*, **4**, 67–89, 1981.
- Tucker, G. E., and R. L. Slingerland, Erosional dynamics, flexural isostasy, and long-lived escarpments: A numerical modeling study, *J. Geophys. Res.*, **99**, 12,229–12,243, 1994.
- Tucker, G. E., and R. L. Slingerland, Predicting sediment flux from fold and thrust belts, *Basin Res.*, **8**, 329–349, 1996.
- Varnes, D. J., Slope movement types and processes, in *Landslides—Analysis and Control*, edited by R. L. Schuster and R. J. Krietzek, *Spec. Rep. Natl. Res. Council. Transp. Res. Board*, **176**, 12–33, 1978.
- Wallace, R. E., Geometry and rates of change of fault-generated range fronts, north-central Nevada, *J. Res. U.S. Geol. Surv.*, **6**, 637–649, 1978.
- Weissel, J. K., and G. D. Karner, Flexural uplift of rift flanks due to mechanical unloading of the lithosphere during extension, *J. Geophys. Res.*, **94**, 13,919–13,950, 1989.
- Weissel, J. K., and M. A. Seidl, Influence of rock strength properties on escarpment retreat across passive continental margins, *Geology*, **25**, 631–634, 1997.
- Wilson, R. C., and D. K. Keefer, Predicting areal limits of earthquake-induced landsliding, *U.S. Geol. Surv. Prof. Pap.*, **1360**, 317–345, 1985.
- Wolman, M. G., and J. P. Miller, Magnitude and frequency of forces in geomorphic processes, *J. Geol.*, **68**, 54–74, 1960.

R. S. Anderson, Department of Earth Sciences, University of California, Santa Cruz, CA 95064.

A. L. Densmore, Department of Geology, Trinity College, Dublin 2, Ireland. (e-mail: densmora@tcd.ie)

M. A. Ellis, Center for Earthquake Research and Information, University of Memphis, Memphis, TN 38152. (e-mail: ellis@ceri.memphis.edu)

(Received March 5, 1997; revised January 13, 1998; accepted January 22, 1998.)